Materials Horizons

Polaron absorption in aligned conjugated polymer films: Breakdown of adiabatic treatments and going beyond the conventional mid-gap state model

Journal:	*Materials Horizons*
Manuscript ID	MH-COM-08-2023-001278.R1
Article Type:	Communication
Date Submitted by the Author:	29-Oct-2023
Complete List of Authors:	LeCroy, Garrett; Stanford University, Materials Science and Engineering Ghosh, Raja; University of California San Diego, Chemistry and Biochemistry Untilova, Viktoriia; Institut Charles Sadron, CNRS Guio, Lorenzo; University of Washington, Department of Materials Science and Engineering Stone, Kevin; SLAC National Accelerator Laboratory, SSRL Brinkmann, Martin; CNRS - Université de Strasbourg, Institut Charles Sadron Luscombe, Christine; Okinawa Institute of Science and Technology (OIST), pi-Conjugated Polymer Unit Spano, Frank; Temple University Salleo, Alberto; Stanford University, Materials Science and Engineering

New Concepts Statement

We present the first experimental quantification of intra- and intermolecular polarized absorption components for polarons in a polymer organic semiconductor (OSC). Mid-IR polaron absorption in OSCs serves as a sensitive probe of material disorder at sub-nanometer length scales, and the correct interpretation of absorption features is critical for development of structure-property relations. Conventional adiabatic interpretations based on the Born-Oppenheimer approximation predict two mid-IR transitions arising from mid-gap electronic states: 1) an intramolecular-polarized peak (P_1) corresponding to a transition to the lowest energy mid-gap state and 2) a lower energy intermolecular-polarized peak (A) arising from charge-transfer between neighboring chains. However, these predictions had never been experimentally resolved until this work. Here, we unambiguously resolve the intra- and intermolecular polarized absorption components through sensitive polarized IR spectroscopy alongside structural characterization to quantify molecular orientation. The experimental results are discrepant with the conventional, adiabatic treatments, as we find the peak A band has a substantial intramolecular component. Instead, the results are consistent with the predictions of a nonadiabatic treatment that incorporates nuclear kinetic energy effects in charge-phonon coupling within a Holstein-style Hamiltonian. This work shows that a nonadiabatic treatment is necessary to interpret IR absorption spectrum and probe material disorder and polaron coherence lengths.

Journal Name

ARTICLE TYPE

Cite this: DOI: 00.0000/xxxxxxxxxx

Polaron absorption in aligned conjugated polymer films: Breakdown of adiabatic treatments and going beyond the conventional mid-gap state model†

Garrett LeCroy,[a] Raja Ghosh[b], Viktoriia Untilova[c], Lorenzo Guio[d], Kevin H. Stone[e], Martin Brinkmann[c], Christine Luscombe[f], Frank C. Spano*[g], and Alberto Salleo*[a]

Received Date
Accepted Date

DOI: 00.0000/xxxxxxxxxx

This study provides the first experimental polarized intermolecular and intramolecular optical absorption components of field-induced polarons in regioregular poly(3-hexylthiophene-2,5-diyl), rr-P3HT, a polymer semiconductor. Highly aligned rr-P3HT thin films were prepared by a high temperature shear-alignment process that orients polymer backbones along the shearing direction. rr-P3HT in-plane molecular orientation was measured by electron diffraction, and out-of-plane orientation was measured through series of synchrotron X-ray scattering techniques. Then, with molecular orientation quantified, polarized charge modulation spectroscopy was used to probe mid-IR polaron absorption in the $\hbar\omega$ = 0.075 - 0.75 eV range and unambiguously assign intermolecular and intramolecular optical absorption components of hole polarons in rr-P3HT. This data represents the first experimental quantification of these polarized components and allowed long-standing theoretical predictions to be compared to experimental results. The experimental data is discrepant with predictions of polaron absorption based on an adiabatic framework that works under the Born-Oppenheimer approximation, but the data is entirely consistent with a more recent nonadiabatic treatment of absorption based on a modified Holstein Hamiltonian. This nonadiabatic treatment was used to show that both intermolecular and intramolecular polaron coherence break down at lengths scales significantly smaller than estimated structural coherence in either direction. This strongly suggests that polaron delocalization is fundamentally limited by energetic disorder in rr-P3HT.

1 Introduction

Electronic charge carriers in organic semiconductors (OSCs) display strong electron-phonon coupling that result in carriers dressed with lattice nuclear displacements. The resulting quasiparticle, a polaron, can have significant spatial localization and typically moves via thermally activated hopping transport [1,2]. Polaron interactions with OSC lattices yield a rich variety of photophysical properties that manifest as sub-band gap absorption features. Numerous theoretical methods including semi-empirical Hartree-Fock methods [3–5], Holstein-style Hamiltonians [6–8], and Density-Functional-Theory (DFT) [9–11] have been used to interpret these absorption features.

The picture presented by the semi-empirical methods has been influential across a wide variety of systems [12–20]. In this interpretation, the adiabatic treatment of a single, nondegenerate ground state polaron on a one-dimensional π-conjugated polymeric OSC yields two mid-gap states: one slightly above the valance band edge and one slightly below the conduction band edge. This is the "mid-gap" state model, and these new states appear in the material band-gap due to nuclear relaxation associated with the aromatic-quinoidal stretching mode of $\hbar\omega_{vib} \approx 0.17$ eV.[4] Two dimensional interactions, such as polymer interchain π-orbital overlap, create level splitting of these mid-gap features [5,17,18,21], and this splitting gives rise to a low energy optical transition ($\hbar\omega$ <0.2

[a] Department of Materials Science and Engineering, Stanford University, Stanford, CA 94305, United States
[b] Department of Chemistry and Biochemistry, University of California San Diego, La Jolla, CA 92037, United States
[c] Université de Strasbourg, CNRS, ICS UPR 22, F-67000 Strasbourg, France
[d] Department of Materials Science and Engineering, University of Washington, Seattle, WA, United States
[e] Stanford Synchrotron Radiation Lightsource, SLAC National Accelerator Laboratory, Menlo Park, California 94025, United States
[f] pi-Conjugated Polymers Unit, Okinawa Institute of Science and Technology, Onna, Okinawa 904–0495, Japan
[g] Department of Chemistry, Temple University, Philadelphia, Pennsylvania 19122, United States
* francis.spano@temple.edu; asalleo@stanford.edu

† Electronic Supplementary Information (ESI,†) available: Experimental details on polymer synthesis, electron diffraction, X-ray scattering, and charge modulation spectroscopy are provided in the supporting information. Supplemental notes on the derivation of molecular orientation geometric adjustments and polaron absorption modeling are also provided in the supporting information. See DOI: 00.0000/00000000.

eV) historically termed the charge-transfer (CT) or delocalized-polaron (DP1) peak[17–19,21]. The low energy peak is interpreted to arise purely from interchain interactions that result in a transition dipole moment (TDM) polarized along the interchain packing axis[5,17]. The mechanism for mid-gap state polaron absorption is depicted schematically in Figure 1, where the interchain polarized nature of CT/DP1 is shown.

However, more recent DFT work questions the assignment and physical origin of polaron mid-gap states even under an adiabatic approximation[9–11]. Particularly, DFT methodologies that incorporate a mean-field level of Coulombic interaction between hole polarons and electrons suggest a strikingly different occupation scheme of mid-gap states compared to previous literature[9,22]. Furthermore, adiabatic treatments tacitly work under the Born-Oppenheimer approximation, but the kinetic energies of vibrational modes responsible for charge-phonon coupling in OSCs are not negligible, as has been demonstrated for Frenkel excitons in π-conjugated systems where electronic degrees of freedom are strongly linked to select phonon modes[23–28]. Significant nuclear vibrational energies necessitate nonadiabatic treatments. Indeed, incorporating nonadiabatic effects into polaron absorption and transport can explain some ultrafast dynamics in charge-transfer blends and neat polythiophenes, where charge-transfer dynamics are mediated by time scales associated with the aromatic-quinoidal stretch ($\approx$ 23 fs)[29,30]. Furthermore, nonadiabatic theoretical treatments based on a modified version of the Holstein Hamiltonian predict a different interpretation of the low energy absorption peak (i.e. the formerly assigned CT or DP1 peak)[6,31]. These treatments suggest this low energy peak (assigned peak "**A**", and referred to as such in this manuscript), arises from interchain transitions, in agreement with the interpretation from adiabatic approaches, *and* intrachain transitions, a stark departure from previous adiabatic calculations[6,32]. This discrepancy necessitates experimental confirmation of intrachain and interchain polaron TDMs ($\boldsymbol{\mu}_{\parallel}$ and $\boldsymbol{\mu}_{\perp}$ respectively).

The correct interpretation of the origin of this low energy absorption feature bears fundamental consequences on the validity of the Born-Oppenheimer approximation in treating the optical excitations of polarons in polymeric OSCs. Furthermore, the mid-IR absorption spectra of polarons on polymers can provide crucial information connecting local (sub-nanometer) energetic and structural order to polaron delocalization and charge transport[6,7,32–34], and the low energy peak **A** has been used previously as an indirect measure of polaron interchain interaction strength[14,17–21]. The validity of using peak **A** to probe interchain polaron interactions is entirely dependent on understanding the polarized TDM contributions to this peak. Thus, in addition to expanding fundamental understanding of nonadiabatic effects on polaron photophysics in polymeric OSCs, the correct assignment of polaron absorption features is vital for structure-property investigations.

A significant experimental challenge in validating any treatment of polaron absorption is the ability to isolate interchain and intrachain absorption contributions. In this work, intrachain and interchain mid-IR polaron absorption components are unambiguously determined in shear-aligned regioregular poly(3-hexylthiophene-2,5-diyl), P3HT,[35] by polarized charge modulation spectroscopy (CMS). We show that the polarized absorption spectra are entirely consistent with a nonadiabatic theoretical framework of polaron absorption based on a modified Holstein Hamiltonian[6,7]. Furthermore, we show that the low energy polaron absorption feature of peak **A** comprises substantial interchain *and* intrachain polarized absorption components, where the contribution of the intrachain TDM cannot be ignored. This last observation makes it impossible to reconcile these experiments with the traditionally-used adiabatic treatment of polaron absorption and indicates that nonadiabatic treatments are necessary.

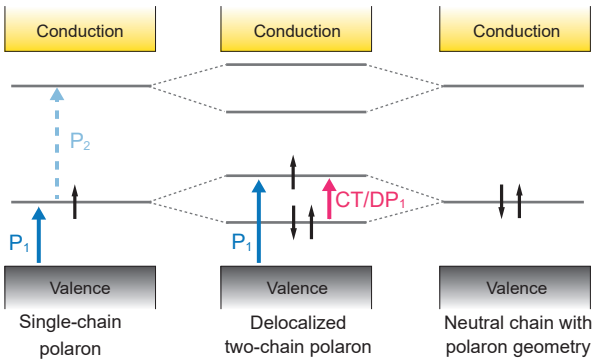

Fig. 1 Schematic showing the mid-gap polaron electronic states based on adiabatic treatments[5,17,18,21]. A polaron confined to a single chain (left panel) creates two mid-gap states, one empty and one singly occupied, with a low energy intrachain transition P1 in the mid-IR and a higher energy transition P2 in the near-IR. Central panel depicts the splitting of mid-gap states induced by interchain interactions. Splitting within the lower mid-gap state gives rise to an interchain polarized, low-energy transition DP1 or CT. It should be noted that the peak assignment presented in this schematic is questioned by more current DFT work[9–11], but this picture has remained important for experimental interpretation[12–20].

2 Results and discussion

2.1 Quantifying molecular orientation

The P3HT (Fig. 2a) employed in this work had perfect regioregularity (>99%, within measurement error) and a high enough molecular weight (M_n = 37 kg mol^{-1}) to be relevant for electronic device applications (Section S1.1 ESI†). P3HT thin films have a semicrystalline microstructure with three relevant crystal stacking axes shown in Fig. 2b: the a-axis lamellar stacking arises from ordering along polymer side-chains, the c-axis backbone stacking arises from coherence of monomer repeat units, and the b-axis π-stacking arises from ordering induced by π-molecular orbital overlap. The crystalline regions comprise 2-dimensional sheets of polymers with ordering in the c- and b-directions, and these sheets stack in the lamellar direction to form 3-dimensional crystals.

Polymer chains were shear-aligned to produce highly in-plane anisotropic films with chains largely aligned along the shearing direction according to methods previously reported by Hamidi-Sakr et al.[37,38]. Polymer backbone (c-axis) orientations then have a narrow distribution about a single direction, and this alignment is shown schematically in Fig. 2c for two limiting cases of poly-

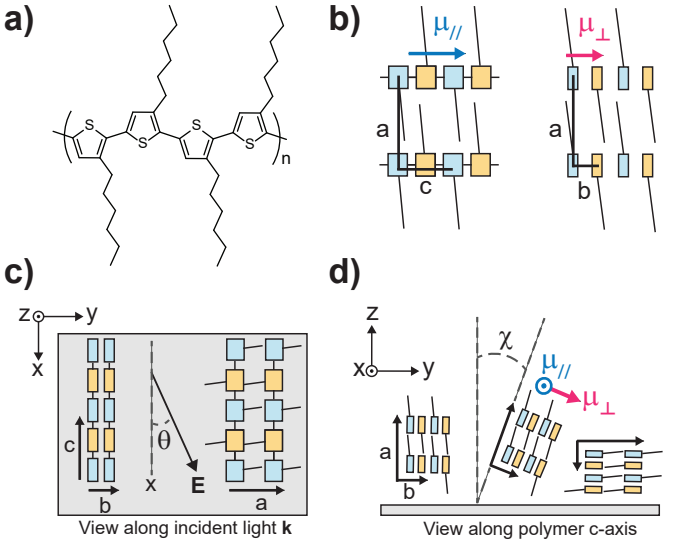

Fig. 2 Polymer structure and definitions of polymer orientation. a) Chemical structure of regioregular P3HT. b) Schematic of approximate polymer crystalline packing[36] shows the lamellar stacking (a-axis), backbone stacking (c-axis), and π-stacking (b-axis) directions. The intrachain TDM, $\boldsymbol{\mu}_{\parallel}$, is oriented along the backbone c-axis, and the interchain TDM, $\boldsymbol{\mu}_{\perp}$, is oriented along the π-stacking b-axis. c) View along the incident light wavevector, k, as seen in optical absorption measurements of polymer films. The incident light electric field vector, E, is defined by the angle θ to the polymer c-axis. Two limiting cases of P3HT orientation with respect to the substrate are shown where the a-axis is normal to the substrate in the edge-on configuration and the a-axis is parallel to the substrate in the face-on configuration. The actual orientation distribution comprises a range of out-of-plane crystallite orientations. d) View along the polymer c-axis of aligned polymer films. Out-of-plane crystallite orientation is defined by polar angle χ between the substrate normal and crystallite a-axis.

mer orientation with respect to the substrate. The polymer crystalline texture thus exhibits a defined in-plane orientation with $\boldsymbol{\mu}_{\parallel}$ oriented along a single direction, but a possible range of out-of-plane orientations such that $\boldsymbol{\mu}_{\perp}$ has an orientation distribution that is not necessarily limited to the two extremes of out-of-plane orientation shown in Fig. 2c.

Fig. 2d shows the definition of out-of-plane crystallite orientation used in this work, where the polar angle χ defines the a-axis orientation relative to the substrate normal. Crystallite orientations form a distribution, $I(\chi)$, that ranges from fully face-on, $\chi = 90°$, to fully edge-on, $\chi = 0°$, as shown by X-ray pole figure analysis of the lamellar (100) peak in Fig. 3a. The pole figure was constructed quantitatively according to existing methods (Section S2.2 ESI†)[39]. Briefly, the (100) peak intensity as a function of polar angle was measured by grazing incidence X-ray scattering and then stitched with a specular diffraction rocking curve. The latter measurement is necessary to capture the highly oriented edge-on crystallite fraction present at the substrate interface ($\chi < 0.01°$)[40], where charges probed by CMS reside. The sharp peak at $\chi \sim 90°$ is caused by the highly oriented face-on crystallite population. We assume that, except for the highly-oriented fractions located at the substrate interface, the remainder of the crystallite distribution is uniform throughout the film, and thus the pole figure is representative of the interfacial distribution probed by CMS.

Fig. 3b shows electron diffraction data used to assess backbone (c-axis) alignment and in-plane orientation. Sharp diffraction peaks associated with polymer backbone (002) and (h02) planes are present in the alignment direction. Additionally, sharp equatorial lamellar (h00) peaks appear alongside the π-stacking (020) peak, showing films comprise edge-on and face-on domains with the polymer chain axis oriented in the alignment direction[41]. Fig. 3c shows electron diffraction data of the (002) backbone peak as a function of azimuthal angle, ϕ. The intensity of this diffraction peak as a function of ϕ is representative of the polymer in-plane orientation distribution, $F(\phi)$. There is some misorientation of polymer chains about the alignment axis as evidenced by the breadth in the (002) diffraction peak, though this breadth is small at $\sim \pm 7°$ about the nominal alignment direction.

Polymer chain alignment was additionally verified with polarized FT-IR absorbance shown in Fig. S7 ESI†. Polarized FT-IR absorbance measured TDMs oriented along the polymer backbone, namely a C=C stretching mode at $\nu_{a,\,C=C}$=1510 cm^{-1} and a thiophene =C-H stretching mode at $\nu_{=C\text{-}H}$=3050 cm^{-1}[42–44]. The amplitudes of these modes show large dichroic ratios (Table S3 ESI†) and a $\cos^2(\theta)$ dependence on incident light orientation, where θ is described in Fig. 2c. This is the expected functional dependence of absorption for highly oriented polymer backbones (see Equation S27 ESI†). Absorbance peaks between 1400 cm^{-1} and 1480 cm^{-1} also have a strong polarization dependence (Fig. S7 ESI†). These modes were not used for orientation analysis in this work since this region comprises overlapping modes of both lower energy C=C vibrations (1449 cm^{-1}) and CH_2 and CH_3 bending modes of the alkyl side chains (1455 cm^{-1} and 1465 cm^{-1})[42,43,45].

2.2 Polarized CMS and absorption modeling

2.2.1 Quantifying absorption components

Polarized CMS was performed to measure polaron absorption components, taking advantage of the polymer backbone orientation. CMS probes absorption of field-induced charge carriers by measuring changes in thin-film transmission, ΔT, associated with modulations in film charge density, $\Delta\rho$, in charge density regimes where charge carrier interaction is expected to be low ($\rho_{\text{volume}} \sim 10^{19}$ cm^{-3}, $\sim$1 charge per 100 monomers), and avoids introduction of dopant bands or dopant-polaron interactions (for estimates of charge density, see Section S2.5 ESI†). If the polymer were purely edge-on, the intrachain and interchain polarized CMS spectra would be directly related to the intrachain and interchain TDMs respectively (Section S2.3 ESI†).

Because the films employed in this study comprise crystallites with a range of out-of-plane orientations, additional care is needed to quantify interchain and intrachain polarized absorption components. The measured intrachain and interchain polaron absorption ($\alpha_{\parallel}$ and $\alpha_{\perp}$ respectively) can be quantitatively linked to crystallite orientation, $I(\chi)$, incident light electric field orientation, θ, and the relevant TDM components, $\boldsymbol{\mu}_{\parallel}$ and $\boldsymbol{\mu}_{\perp}$, as shown in Equations 1 and 2 (derivations in Section S2.3 ESI†).

$$\alpha_{\parallel}(\hbar\omega,\theta) \propto \boldsymbol{\mu}_{\parallel}^2 \cos^2(\theta)\left(\int_{\chi=-90^\circ}^{\chi=90^\circ} I(\chi)\, d\chi\right)^2 \quad (1)$$

$$\alpha_{\perp}(\hbar\omega,\theta) \propto \boldsymbol{\mu}_{\perp}^2 \sin^2(\theta)\left(\int_{\chi=-90^\circ}^{\chi=90^\circ} I(\chi)\cos(\chi)\, d\chi\right)^2 \quad (2)$$

While the intrachain polarized absorption component has no dependency on out-of-plane crystallite orientation (Equation 1 and S23 ESI†), the interchain polarized absorption component has a $\cos^2(\chi)$ type dependence (Equation 2 and Equation S24 ESI†). For a perfectly face-on crystallite, $\boldsymbol{\mu}_{\perp}$ is orthogonal to the incident light electric field vector, **E**, and the associated absorption is dark in CMS. This means that, unless a thin film is perfectly edge-on orientated such that $I(\chi)$ is a delta function centered at $\chi = 0^\circ$, the measured interchain polaron absorption component is necessarily weakened purely due to geometric effects of crystallite orientation. Since a key goal of this work was to quantify interchain and intrachain absorption components, we make an adjustment based on the measured $I(\chi)$ distribution to the measured interchain polaron absorption component that accounts for the relative weakening due to crystallite orientation. Full details of this adjustment and derivation of relevant equations are given in Section S2.3 ESI†.

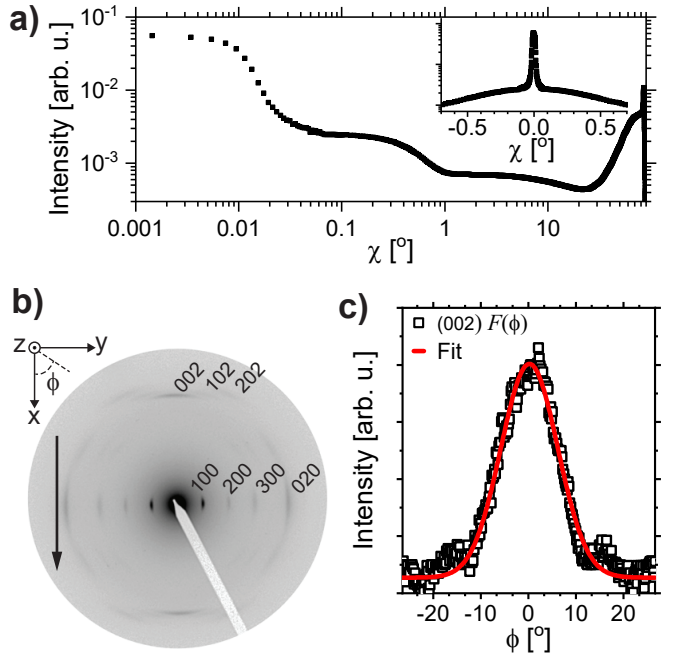

Fig. 3 In-plane and out-of-plane polymer crystallite orientation analysis. a) Pole figure of the (100) lamellar peak used to define polymer out-of-plane orientation distribution $I(\chi)$. Inset shows data near $\chi = 0^\circ$ on a linear x-scale. b) Electron diffraction data with labelled diffraction peaks. Arrow shows shearing and nominal polymer alignment direction. Coordinate axes as defined in Fig. 2 shown, along with the definition of polymer backbone azimuthal angle, ϕ. c) Polymer backbone (002) diffraction intensity as a function of azimuthal angle used to define polymer in-plane orientation distribution $F(\phi)$. A Gaussian fit is shown that was used to estimate misorientation of polymer chains.

2.2.2 CMS and model fitting of polaron spectra

After making the adjustments necessary to account for crystallite out-of-plane orientation effects, the measured charge modulation spectrum for the interchain absorption component is scaled up by a factor of 2.45. This scaling gives the absorption that would be expected for a perfectly edge-on film where none of the interchain absorption component is weakened due to out-of-plane crystallite orientation effects. Combining the experimental intrachain and adjusted interchain spectra allows quantification of the relative intensities of the polarized absorption components for polarons in P3HT and allows for simultaneous absorption model fitting to both components without separate scaling. To the best of our knowledge, this is the first time a quantitative comparison of these absorption components has been reported.

Model fits were performed using a Holstein-style Hamiltonian and basis set described previously[6,7,33]. Polaron-polaron interactions are not considered in this work, as these energies are expected to be negligible due to the low charge densities accessed in CMS devices (~1 polaron per 100 monomers, Section S2.5 ESI†). For an M×N aggregate consisting of N polymer chains each containing M thiophene units, the resulting Hamiltonian, H, comprises two main components: 1) H_0, which captures hole polaron hopping, vibrational excitation, and charge-phonon coupling, and 2) H_{dis}, which captures energetic disorder. The Hamiltonian is shown in Equation (3)[6].

$$H = H_0 + H_{\text{dis}} \quad (3)$$

where,

$$\begin{aligned} H_0 = {} & \textstyle\sum_{m=1}^{M-1}\sum_{n=1}^{N} t_{\text{intra}}\left(d_{m+1,n}^{\dagger} d_{m,n} + \text{h.c.}\right) + \\ & \textstyle\sum_{m=1}^{M}\sum_{n=1}^{N-1} t_{\text{inter}}\left(d_{m,n+1}^{\dagger} d_{m,n} + \text{h.c.}\right) + \\ & \hbar\omega_{\text{vib}} \textstyle\sum_{m=1}^{M}\sum_{n=1}^{N} b_{m,n}^{\dagger} b_{m,n} + \\ & \hbar\omega_{\text{vib}} \textstyle\sum_{m=1}^{M}\sum_{n=1}^{N} \left(\lambda\left(b_{m,n}^{\dagger} + b_{m,n}\right) + \lambda^2\right) d_{m,n}^{\dagger} d_{m,n} \end{aligned} \quad (4)$$

and

$$H_{\text{dis}} = \sum_{m=1}^{M}\sum_{n=1}^{N} \varepsilon_m d_{m,n}^{\dagger} d_{m,n} \quad (5)$$

In equations (4) and (5), $d_{m,n}^{\dagger}$ and $d_{m,n}$ represent the raising and lowering Fermion operators respectively for a single hole on the m^{th} monomer of the n^{th} chain. Here, a hole represents a half-filled local thiophene HOMO, and h.c. represents the Hermitian conjugate. $b_{m,n}^{\dagger}$ and $b_{m,n}$ represent the raising and lowering Boson operators for vibrational quanta. The first two terms in Equation (4) account for local hole energy and electronic coupling, with the intrachain (interchain) transfer integrals of t_{intra} (t_{inter}). Vibrational excitation involving the aromatic-quinoidal stretch with $\hbar\omega_{\text{vib}}$ = 0.17 eV is accounted for in the third term. The fourth term represents local charge-phonon coupling, quantified by the Huang-Rhys factor, λ^2, which is approximately one for molecular thiophene[6]. $\hbar\omega_{\text{vib}}\lambda^2$ is the nuclear relaxation associated with

polaron formation on a given site[6]. Disorder is incorporated as diagonal disorder in Equation (5) by adding a random energetic offset, ε_m, to each site determined from a Gaussian distribution, $P(\varepsilon_m)$, with breadth, σ_{dis}, of site energy offsets given in Equation (6).

$$P(\varepsilon_m) = \left(2\pi\sigma_{\text{dis}}^2\right)^{\frac{-1}{2}} \exp\left(-\varepsilon_m^2/(2\sigma_{\text{dis}}^2)\right) \quad (6)$$

In this work, a 10 thiophene by 4 chain P3HT π-stack (M = 10, N = 4) was used as a model aggregate, with t_{intra} = -0.4 eV and t_{inter} = -0.11 eV, in line with previous applications of the Hamiltonian in Equation (3)[32,34]. Energetic disorder was modeled as short-range in the intrachain direction, where each monomer along a single chain could have a different site energy, and long-range in the interchain π-stacking direction, where the m^{th} monomer site energy is identical across the 4 chains. This leads the energetic offset term, ε_m, in Equations 5 and 6 to only have a dependence on the monomer position, m. A Gaussian breadth of σ_{dis} = 0.3 eV was used for the energetic offset distribution in Equation (6). Limiting the stack to four chains is a way of incorporating shorter-range interchain disorder. Including more than (fewer than) four chains would red-shift (blue-shift) the b-axis interchain polarized component of peak **A** away from the measured peak. Details on the calculation of absorption spectra are presented in Section S2.4 ESI†.

Fig. 4a,b show, on the same scale, the intrachain and adjusted interchain polarized CMS components respectively, along with model fits to the spectra. Once we correct for the crystallite out-of-plane orientation distribution, both spectra are fit simultaneously without any scaling factor needed. Absorption cross sections, σ, are comparable to those in similar molecular weight P3HT processed from 1,2,4-trichlorobenzene that forms structurally ordered films[46], and higher than those of lower molecular weight P3HT and some high mobility donor-acceptor polymers[18,47], suggesting that polarons occupy structurally ordered environments. The intermolecular polarized spectrum has a residual background at $\hbar\omega$ >0.25 eV which is likely from the disordered film fraction and slight misorientation of crystallites[37].

Our coarse-grained theoretical treatment of polaron absorption captures the broad, electronic polaron transitions. The model does not account for the very sharp infrared active transitions that appear in the spectrum for $\hbar\omega < 0.2$ eV (insets in Fig. 4a,b). Such Fano-resonances arise from antiresonance interference between narrow linewidth vibrational transitions and broad polaron electronic transitions[48]. Nevertheless, our treatment captures the general envelope of the polaron electronic transitions. We verify the reliability of our spectral geometric adjustments by using the model fits for the pure intra- and interchain components (Fig. 4a,b) and adjusting model fits according to Equations S27 and S28 ESI†, for intermediate polarization angles to verify the experimental results. Fig. 4c shows the adjusted model fits for two additional polarization angles (additional CMS sample shown in Fig. S8 ESI†). The model fits capture the relative intensities and spectral shapes qualitatively well.

2.2.3 Interpreting polaron absorption

The spectral region of $\hbar\omega < 0.20$ eV comprises peak **A** (highlighted in Fig. 4a,b). This spectral region represents the formerly assigned DP1 or CT peaks as shown in Fig. 1. The experimental results show that this peak has a significant interchain spectral weight component (Table S2 ESI†). However, the intrachain component in this spectral region is also significant, representing nearly half the spectral weight of this peak, and this is discrepant with predictions of the adiabatic mid-gap state picture shown in Figure 1.[5,14,16–18] The spectra in Fig. 4a,b matches closely with previous theoretical predictions of Ghosh et al.[33], and display qualitatively similar interchain and intrachain absorption components as estimated by Chew et al. on CMS measurements of P3HT[34]. However, we emphasize that previous experimental work and modeling was based on data acquired from spin-coated thin films, which have in-plane cylindrical symmetry, and thus do not allow for quantification or unambiguous measurement of the polarized absorption components. Therefore, this work represents the first time that these absorption components have been experimentally resolved.

The experimental and simulated spectra highlight other subtle points of polaron absorption in P3HT. The large oscillator strength of peak **A** in both the intra- and interchain components can be interpreted as arising from an interplay between charge transfer and vibronic coupling. The red-shift of 37 meV (∼300 cm^{-1}) of the interchain component of peak **A** (Fig. 4b) compared to the intrachain component (Fig. 4a) reflects the much weaker inter- vs intra-chain electronic coupling ($|t_{\text{intra}}| > |t_{\text{inter}}|$) matching well with previous predictions using the same Holstein-style Hamiltonian employed here[33]. As shown in Figure S9 ESI†, with increasing polaron localization the energy of peak **A** tends towards the aromatic-quinoidal vibration ($\hbar\omega$=0.17 eV) which can be understood as a form of Herzberg-Teller coupling[32,33,49]. The intensity of peak **A** is directly linked to the nonadiabatic charge-phonon coupling introduced in the third and fourth terms of Equation 4. Indeed, removal of these terms (i.e. removing vibronic coupling effects) destroys the separation of peak **A** and peak **B** as is shown in Figure S9 ESI†.

Fig. 4d shows the coherence function (Equation S35 ESI†) of the ground state polaron wavefunction as found from the model fits shown in Fig. 4a,b. Coherence is greater in the intrachain direction at 5.2 monomer sites (∼1.62 nm), which is smaller than the polymer persistence length (l_p ∼3 nm in solution)[50]. The interchain coherence is smaller at 3.5 monomer sites (∼0.96 nm). This yields a polaron "size" of ∼1.55 nm^2. Compared to sizes extracted from CMS measurements on a similar dielectric interface, the size here is significantly larger than that of spin-coated P3HT, where an effective polaron size of ∼0.44 nm^2 was found[34]. However, passivation of oxide dielectric interfaces is known to reduce energetic disorder in OSC thin films. The films employed in this study do not have any dielectric surface modifications due to the polymer aligning process used, and the polaron size is smaller than that of spin-coated P3HT on a silane modified SiO_2 interface, where an intrachain (interchain) coherence of 5.2 (5.0) monomer sites was found for a polaron size of ∼2.98 nm^2[34]. This suggests

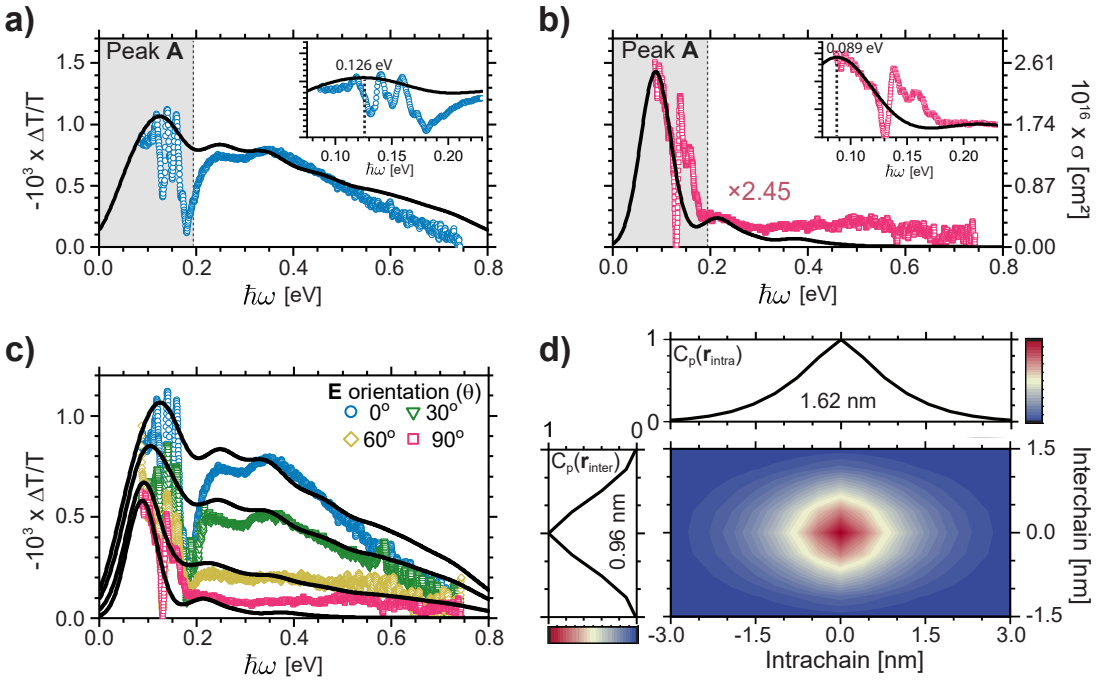

Fig. 4 Polarized CMS experimental results and model fits. On the ordinate same scale, a) Intrachain (E at $\theta = 0°$) and b) Interchain (E at $\theta = 90°$) CMS spectra (symbols) and model fits (solid lines). The peak **A** region is highlighted, and the interchain component has been multiplied by 2.45 to adjust for crystallite out-of-plane orientation effects on absorption (Equation S30 ESI†). Data is shown in units of both $\Delta T/T$ and absorption cross section, σ, as calculated from Equation S2 ESI†. Insets show spectral region of $\hbar\omega < 0.20$ eV and sharp anti-resonance dips in the absorption spectra. Dashed vertical lines in insets show center of Peak **A** absorption with labels. c) CMS data (symbols) at various E orientations relative to polymer chain alignment (see Fig. 2) with combinations (solid lines) of intrachain and interchain fits according to Equations S27 and S28 ESI†. Component fits are shown in Fig. S8 ESI†. d) Two-dimensional ground state polaron coherence function, $C_p(r)$, defined in Equation S35 ESI†, as found from fits of the polarized CMS data. $C_p(r)$ is shown as a function of intrachain and interchain position for a P3HT π-stack. One-dimensional intrachain and interchain coherence shown on the sides of the two-dimensional data, along with estimated polaron coherence lengths of 0.96 nm interchain and 1.62 nm intrachain based on the sum shown in Equation S36 ESI†.

that, while mesoscale polymer alignment can certainly increase polaron delocalization, particularly in the interchain direction, reducing energetic disorder may be a more important contributor to increasing polaron delocalization.

2.3 Discussion of polaron coherence limits

We have shown here that a nonadiabatic Holstein-style model accounts for both the interchain and intrachain mid-IR absorption spectrum of polarons in aligned P3HT films. Models based on an adiabatic treatment of the aromatic-quinoidal vibration have attributed the low-energy absorption peak (DP1, CT, or **A**) entirely to interchain charge-transfer involving a low-energy mid-gap state[5,16,17]. While this understanding has underpinned a number of experimental interpretations[16–19,21], this treatment cannot account for the substantial intrachain absorption component measured here. Moreover, the nonadiabatic Holstein model employed here emphasizes the importance of vibronic coupling in polaron transitions which is absent in adiabatic treatments of interchain absorption. For both inter- and intrachain components the amplitude of the peak **A** diminishes and tends towards the frequency, ω_{vib}, of the aromatic-quinoidal mode ($\hbar\omega_{vib}$ = 0.17 eV) as the polaron localizes (Figure S9 ESI†)[32,33], which is corroborated by numerous studies of chemically doped P3HT where the peak **A** lies close to ω_{vib}[51–53]. Nonadiabatic vibronic coupling appears essential to capturing the appropriate physics of charge motion and optical absorption in π-conjugated systems as has been shown for exciton absorption and ultra-fast dynamics of polarons in charge-transfer blend systems[23,24,26,27,29,30].

Having verified that the nonadiabatic Holstein model we use to interpret mid-IR polaron absorption spectra is consistent with our polarized absorption measurements, we are able to gain insights on limits of polaron coherence in P3HT. In similar aligned films as used in this study, crystallites have been measured with structural coherence lengths along the chain direction of $l_{c,\,\mathrm{chain}}$ ~14 nm,[37,41,54] and the X-ray scattering of this work gives a π-stacking coherence length of $l_{c,\,\pi}$ ~6.5 nm (Fig. S6 ESI†). Comparing these experimentally measured structural coherence lengths to the calculated polaron coherence lengths based on CMS results (1.62 nm intrachain and 0.96 nm interchain, Fig. 4) reveals that polarons are much smaller than the structural coherence in both the intrachain and interchain directions at less than ~15% of the structural coherence in either direction. The significant localization of the polaron in P3HT when compared to both crystallite structural coherence and polymer solution persistence length (l_p ~3 nm)[50] matches well with previous interpretations of relatively large nanoscale disorder present in P3HT crystallites[34].

This is also apparent from comparison of estimated polaron

delocalization lengths on structurally disorder-free chains where coherence extends up to 10 monomer sites[55]. Despite having films with ordered microstructures in this work, the polaron coherence length along the polymer backbone is no greater than that found for spin-coated P3HT films, regardless of dielectric surface modification[34]. Furthermore, comparing the interchain polaron coherence lengths found in this work with that of spin-coated P3HT on a silane-modified oxide shows that the interchain polaron coherence is lower in the aligned P3HT films of this work ($\sim$3.5 compared to $\sim$5 monomer units)[34], despite the improved mesoscale ordering of the aligned films. Some care should be used in interpreting interchain structural order, as, despite the relatively large interchain structural coherence found in aligned P3HT films, there is still significant structural disorder in this direction, as even room-temperature thermal fluctuations of OSC lattices can induce paracrystallinity on the order of 5%[56], and we estimate a paracrystallinity of 9.2% (Fig. S6 ESI†), in line with other higher molecular weight P3HT[57,58]. Nevertheless, the decreased interchain polaron coherence length in this work compared with that of P3HT with less energetic disorder[34] further shows that structural coherence is not the key limiting factor to polaron coherence.

Shear-alignment results in P3HT films with relatively long interacting conjugation segments as evidenced by a low H-aggregate interchain exciton bandwidth ($\sim$36 meV Fig. S4 ESI†), but this value remains similar to values of P3HT spin-coated from high boiling point solvents[15,59]. This again suggests that, despite the remarkable macroscopic and mesoscopic ordering of our shear-aligned P3HT films, factors outside of structural coherence disrupt polymer conjugation and polaron/exciton coherence.

Indeed, these results strongly suggest that, at least in the backbone direction of P3HT, local energetic disorder and dynamic disorder associated with thermal fluctuations of polymer lattice sites govern charge localization, rather than static structural disorder. We base this conclusion on the observation that intrachain polaron delocalization in P3HT films with a lower degree of intrachain structural coherence is similar to the delocalization of the ordered shear-aligned films in this work[34]. Energetic disorder has been shown to be a limiting factor in delocalization of polarons in π-conjugated systems via Anderson-like localization[8,32,60,61]. We note that this differs from some interpretations of exciton localization in π-conjugated systems where the localization is attributed to strong coupling between the excited states and intramolecular phonon modes[27,28,62,63], but this is likely not surprising as the exciton excited state is not equivalent to the polaronic ground state, so different localization mechanisms could be at play. Furthermore, P3HT is known to have relatively large intramolecular disorder due to subtle conformational changes along the polymer backbone[64], and thus the relatively small ratio of polaron coherence to structural coherence found in this work agrees well with the known energetic disorder present in P3HT. Based on this, we conclude that the polaron size estimated in the shear aligned films of this work and in optimized spin-coated P3HT films is near the upper limit of polaron delocalization in room temperature P3HT. Indeed, the shear aligned-films represent one of the most ordered form of P3HT observed to-date. Thus, further intrachain polaron delocalization in a semiflexible polymer such as P3HT is limited by the inevitable energetic and likely dynamic disorder associated with the polymer backbone. Furthermore, interchain delocalization is limited due to reduction of interchain order from both static and dynamic paracrystallinity effects[56,65]. Inducing further intrachain delocalization, which may be beneficial to transport, would have to involve changes to the structure of the backbone to make it more rigid, such as the introduction of fused rings as is seen in more recent high-mobility organic semiconductors[66].

3 Conclusion

Using shear-aligned P3HT films and polarized CMS, we unambiguously measure for the first time the interchain and intrachain polarized absorption components of polarons in P3HT. We show that optical excitation of polaronic charges in conjugated polymers is discrepant with predictions of an adiabatic mid-gap state model that has been widely adopted to interpret polaron absorption in polymeric π-conjugated systems[12–20]. Furthermore, this study adds further evidence that polaron dynamics and transport operate outside the Born-Oppenheimer approximation due to the strong coupling between electronic motion and nuclear vibrational motion[23,24,26–28,30]. A nonadiabatic treatment based on a Holstein-style Hamiltonian[6,7] was shown to correctly interpret the low-energy features of the absorption spectra. Fitting polarized absorption spectra with this nonadiabatic treatment allows us to discuss fundamental limits of polaron delocalization both along chains and in the π-stacking direction for P3HT. We conclude that delocalization is fundamentally limited by nanoscale energetic and dynamic disorder in P3HT, independent of processing. This shows the importance of optical spectroscopies and appropriate modeling to understand such nanoscale disorder that may not be apparent or measurable by other structural characterization. Furthermore, we can now make use of a validated nonadiabatic interpretation of mid-IR polaron absorption to understand limits of polaron delocalization and effects of nanoscale disorder in wider classes of polymeric OSCs in future work.

Author Contributions

G.L., R.G., F.C.S., and A.S. conceived the project idea. G.L. performed CMS measurements under the supervision of A.S. G.L. and K.H.S. performed X-ray scattering experiments. V.U. performed P3HT shear-alignment under supervision of M.B. L.G. synthesized P3HT under the supervision of C.L. R.G. and F.C.S. performed polaron absorption spectral modeling. G.L., R.G., F.C.S., and A.S. wrote the initial draft. All authors contributed to discussion and review of data.

Conflicts of interest

There are no conflicts to declare.

Acknowledgements

G.L., A.S., C.K.L., and F.C.S. acknowledge the U.S. Department of Energy (DOE), Office of Science, Basic Energy Sciences (BES), under award DE-SC0020046. L.G. acknowledges support from the National Science Foundation (NSF) under award number DMR-

2104234. G.L. acknowledges support from the NSF Graduate Research Fellowship Program under grant DGE-1656518. We acknowledge the support of NVIDIA Corporation with the donation of the Titan V GPU used for this research. The use of Stanford Synchrotron Radiation Lightsource, SLAC National Accelerator Laboratory, is supported by the US DOE, Office of Science, Office of Basic Energy Sciences, under contract no. DE-AC02-76SF00515. M.B. acknowledges support from ANR under contract ANR-17-CE05-0012.

Notes and references

1 N. Sai, P. F. Barbara and K. Leung, *Physical Review Letters*, 2011, **106**, 226403.

2 H. Bässler and A. Köhler, in *Charge Transport in Organic Semiconductors*, Springer Berlin Heidelberg, 2011, pp. 1–65.

3 J. Cornil, D. Beljonne and J. L. Brédas, *The Journal of Chemical Physics*, 1995, **103**, 834–841.

4 J. L. Bredas and G. B. Street, *Accounts of Chemical Research*, 1985, **18**, 309–315.

5 D. Beljonne, J. Cornil, H. Sirringhaus, P. J. Brown, M. Shkunov, R. H. Friend and J. L. Bredas, *Advanced Functional Materials*, 2001, **11**, 229–234.

6 R. Ghosh, C. M. Pochas and F. C. Spano, *The Journal of Physical Chemistry C*, 2016, **120**, 11394–11406.

7 C. M. Pochas and F. C. Spano, *The Journal of Chemical Physics*, 2014, **140**, 244902.

8 O. R. Tozer and W. Barford, *Physical Review B*, 2014, **89**, 155434.

9 G. Heimel, *ACS Central Science*, 2016, **2**, 309–315.

10 I. Zozoulenko, A. Singh, S. K. Singh, V. Gueskine, X. Crispin and M. Berggren, *ACS Applied Polymer Materials*, 2019, **1**, 83–94.

11 I. Sahalianov, J. Hynynen, S. Barlow, S. R. Marder, C. Müller and I. Zozoulenko, *The Journal of Physical Chemistry B*, 2020, **124**, 11280–11293.

12 P. A. Christensen, A. Hamnett, A. R. Hillman, M. J. Swann and S. J. Higgins, *Journal of the Chemical Society, Faraday Transactions*, 1992, **88**, 595–604.

13 M. Fahlman, A. Crispin, X. Crispin, S. K. Henze, M. P. de Jong, W. Osikowicz, C. Tengstedt and W. R. Salaneck, *Journal of Physics: Condensed Matter*, **19**, 183202.

14 X. M. Jiang, R. Österbacka, O. Korovyanko, C. P. An, B. Horovitz, R. A. J. Janssen and Z. V. Vardeny, *Advanced Functional Materials*, 2002, **12**, 587–597.

15 J.-F. Chang, J. Clark, N. Zhao, H. Sirringhaus, D. W. Breiby, J. W. Andreasen, M. M. Nielsen, M. Giles, M. Heeney and I. McCulloch, *Physical Review B*, 2006, **74**, 115318.

16 H. Sirringhaus, P. J. Brown, R. H. Friend, M. M. Nielsen, K. Bechgaard, B. M. W. Langeveld-Voss, A. J. H. Spiering, R. A. J. Janssen, E. W. Meijer, P. Herwig and D. M. De Leeuw, *Nature*, 1999, **401**, 685–688.

17 R. Osterbacka, C. P. An, X. M. Jiang and Z. V. Vardeny, *Science*, 2000, **287**, 839–842.

18 P. J. Brown, H. Sirringhaus, M. Harrison, M. Shkunov and R. H. Friend, *Physical Review B*, 2001, **63**, 125204.

19 P. J. Brown, D. S. Thomas, A. Kohler, J. S. Wilson, J.-S. Kim, C. M. Ramsdale, H. Sirringhaus and R. H. Friend, *Physical Review B*, 2003, **67**, 064203.

20 M. Wohlgenannt, X. M. Jiang and Z. V. Vardeny, *Physical Review B*, 2004, **69**, 241204(R).

21 S. Kahmann, D. Fazzi, G. J. Matt, W. Thiel, M. A. Loi and C. J. Brabec, *The Journal of Physical Chemistry Letters*, 2016, **7**, 4438–4444.

22 S. Winkler, P. Amsalem, J. Frisch, M. Oehzelt, G. Heimel and N. Koch, *Materials Horizons*, 2015, **2**, 427–433.

23 S. Tretiak, A. Saxena, R. L. Martin and A. R. Bishop, *Physical Review Letters*, 2002, **89**, 097402.

24 R. D. Pensack and J. B. Asbury, *The Journal of Physical Chemistry Letters*, 2010, **1**, 2255–2263.

25 T. Nelson, S. Fernandez-Alberti, A. E. Roitberg and S. Tretiak, *Accounts of Chemical Research*, 2014, **47**, 1155–1164.

26 T. R. Nelson, A. J. White, J. A. Bjorgaard, A. E. Sifain, Y. Zhang, B. Nebgen, S. Fernandez-Alberti, D. Mozyrsky, A. E. Roitberg and S. Tretiak, *Chemical Reviews*, 2020, **120**, 2215–2287.

27 N. P. Wells, B. W. Boudouris, M. A. Hillmyer and D. A. Blank, *The Journal of Physical Chemistry C*, 2007, **111**, 15404–15414.

28 N. P. Wells and D. A. Blank, *Physical Review Letters*, 2008, **100**, 086403.

29 A. De Sio, F. Troiani, M. Maiuri, J. Réhault, E. Sommer, J. Lim, S. F. Huelga, M. B. Plenio, C. A. Rozzi, G. Cerullo, E. Molinari and C. Lienau, *Nature Communications*, 2016, **7**, 13742.

30 S. M. Falke, C. A. Rozzi, D. Brida, M. Maiuri, M. Amato, E. Sommer, A. De Sio, A. Rubio, G. Cerullo, E. Molinari and C. Lienau, *Science*, 2014, **344**, 1001–5.

31 T. Holstein, *Annals of Physics*, 1959, **8**, 343–389.

32 R. Ghosh, A. R. Chew, J. Onorato, V. Pakhnyuk, C. K. Luscombe, A. Salleo and F. C. Spano, *The Journal of Physical Chemistry C*, 2018, **122**, 18048–18060.

33 R. Ghosh, C. K. Luscombe, M. Hambsch, S. C. B. Mannsfeld, A. Salleo and F. C. Spano, *Chemistry of Materials*, 2019, **31**, 7033–7045.

34 A. R. Chew, R. Ghosh, V. Pakhnyuk, J. Onorato, E. C. Davidson, R. A. Segalman, C. K. Luscombe, F. C. Spano and A. Salleo, *Advanced Functional Materials*, 2018, **28**, 1804142.

35 H. A. Bronstein and C. K. Luscombe, *Journal of the American Chemical Society*, 2009, **131**, 12894–12895.

36 S. Himmelberger, D. T. Duong, J. E. Northrup, J. Rivnay, F. P. V. Koch, B. S. Beckingham, N. Stingelin, R. A. Segalman, S. C. B. Mannsfeld and A. Salleo, *Advanced Functional Materials*, 2015, **25**, 2616–2624.

37 A. Hamidi-Sakr, L. Biniek, S. Fall and M. Brinkmann, *Advanced Functional Materials*, 2016, **26**, 408–420.

38 A. Hamidi-Sakr, L. Biniek, J.-L. Bantignies, D. Maurin, L. Herrmann, N. Leclerc, P. Lévêque, V. Vijayakumar, N. Zimmermann and M. Brinkmann, *Advanced Functional Materials*, 2017, **27**, 1700173.

39 J. L. Baker, L. H. Jimison, S. Mannsfeld, S. Volkman, S. Yin, V. Subramanian, A. Salleo, A. P. Alivisatos and M. F. Toney, *Langmuir*, 2010, **26**, 9146–9151.

40 L. H. Jimison, S. Himmelberger, D. T. Duong, J. Rivnay, M. F. Toney and A. Salleo, *Journal of Polymer Science Part B: Polymer Physics*, 2013, **51**, 611–620.

41 N. Kayunkid, S. Uttiya and M. Brinkmann, *Macromolecules*, 2010, **43**, 4961–4967.

42 G. Louarn, M. Trznadel, J. P. Buisson, J. Laska, A. Pron, M. Lapkowski and S. Lefrant, *The Journal of Physical Chemistry*, 1996, **100**, 12532–12539.

43 L. Brambilla, C. Capel Ferrón, M. Tommasini, K. Hong, J. T. López Navarrete, V. Hernández and G. Zerbi, *Journal of Raman Spectroscopy*, 2018, **49**, 569–580.

44 M. C. Gurau, D. M. Delongchamp, B. M. Vogel, E. K. Lin, D. A. Fischer, S. Sambasivan and L. J. Richter, *Langmuir*, 2007, **23**, 834–842.

45 L. Brambilla, M. Tommasini, I. Botiz, K. Rahimi, J. O. Agumba, N. Stingelin and G. Zerbi, *Macromolecules*, 2014, **47**, 6730–6739.

46 J.-F. Chang, H. Sirringhaus, M. Giles, M. Heeney and I. McCulloch, *Physical Review B*, 2007, **76**, 205204.

47 E. Williams, T. Ang, Z. Ooi, P. Sonar, T. Lin, W. Neo, J. Song and J. Hobley, *Polymers*, 2014, **7**, 69–90.

48 R. Osterbacka, X. M. Jiang, C. P. An, B. Horovitz and Z. V. Vardeny, *Physical Review Letters*, 2002, **88**, 226401.

49 R. Ghosh and F. C. Spano, *Accounts of Chemical Research*, 2020, **53**, 2201–2211.

50 B. McCulloch, V. Ho, M. Hoarfrost, C. Stanley, C. Do, W. T. Heller and R. A. Segalman, *Macromolecules*, 2013, **46**, 1899–1907.

51 A. R. Chew and A. Salleo, *MRS Communications*, 2017, **7**, 728–734.

52 D. T. Scholes, P. Y. Yee, J. R. Lindemuth, H. Kang, J. Onorato, R. Ghosh, C. K. Luscombe, F. C. Spano, S. H. Tolbert and B. J. Schwartz, *Advanced Functional Materials*, 2017, **27**, 1702654.

53 T. J. Aubry, K. J. Winchell, C. Z. Salamat, V. M. Basile, J. R. Lindemuth, J. M. Stauber, J. C. Axtell, R. M. Kubena, M. D. Phan, M. J. Bird, A. M. Spokoyny, S. H. Tolbert and B. J. Schwartz, *Advanced Functional Materials*, 2020, **30**, 2001800.

54 M. Brinkmann and P. Rannou, *Macromolecules*, 2009, **42**, 1125–1130.

55 J. H. Bombile, M. J. Janik and S. T. Milner, *Physical Chemistry Chemical Physics*, 2018, **20**, 317–331.

56 W. Zhang, J. H. Bombile, A. R. Weisen, R. Xie, R. H. Colby, M. J. Janik, S. T. Milner and E. D. Gomez, *Macromolecular Rapid Communications*, 2019, **40**, 1900134.

57 R. Noriega, J. Rivnay, K. Vandewal, F. P. V. Koch, N. Stingelin, P. Smith, M. F. Toney and A. Salleo, *Nature Materials*, 2013, **12**, 1038–1044.

58 K. Gu, C. R. Snyder, J. Onorato, C. K. Luscombe, A. W. Bosse and Y.-L. Loo, *ACS Macro Letters*, 2018, **7**, 1333–1338.

59 J. Clark, J.-F. Chang, F. C. Spano, R. H. Friend and C. Silva, *Applied Physics Letters*, 2009, **94**, 163306.

60 W. Barford, M. Marcus and O. R. Tozer, *The Journal of Physical Chemistry A*, 2016, **120**, 615–620.

61 P. W. Anderson, *Physical Review*, 1958, **109**, 1492–1505.

62 E. Busby, E. C. Carroll, E. M. Chinn, L. Chang, A. J. Moulé and D. S. Larsen, *The Journal of Physical Chemistry Letters*, 2011, **2**, 2764–2769.

63 W. J. D. Beenken and T. Pullerits, *The Journal of Physical Chemistry B*, 2004, **108**, 6164–6169.

64 A. Thiessen, J. Vogelsang, T. Adachi, F. Steiner, D. Vanden Bout and J. M. Lupton, *Proceedings of the National Academy of Sciences*, 2013, **110**, E3550–E3556.

65 A. Troisi, G. Orlandi and J. E. Anthony, *Chemistry of Materials*, 2005, **17**, 5024–5031.

66 X. Zhang, H. Bronstein, A. J. Kronemeijer, J. Smith, Y. Kim, R. J. Kline, L. J. Richter, T. D. Anthopoulos, H. Sirringhaus, K. Song, M. Heeney, W. Zhang, I. McCulloch and D. M. Delongchamp, *Nature Communications*, 2013, **4**, 2238.